Mapping of biophysical and biochemical properties of coastal tidal wetland habitats with Landsat 8

Nanhuanuowa Zhu,[a,b] Christiaan Van der Tol,[b] Aiping Feng,[a] Li Huang,[a] and Nini Wang[a,*]

[a]Ministry of Ecology and Environment, Satellite Application Center for Ecology and Environment, Beijing, China

[b]University of Twente, Faculty of Geo-Information Science and Earth Observation, Enschede, Netherlands

Abstract. Coastal tidal wetlands are significant and vulnerable aquatic ecosystems. Quantitative remote sensing of biophysical and biochemical properties in coastal tidal wetland habitats through the inversion of physical models has vital practical significance for monitoring ecosystem function, environmental restoration, the global carbon, and nitrogen cycles. The objectives of this research were to map leaf area index (LAI), chlorophyll content, as well as the sensible heat flux, latent heat flux, and productivity in Chongming Dongtan coastal tidal wetland habitats of China and to provide a mapping protocol of biophysical and biochemical properties in Chongming Dongtan wetland for environmental protection and restoration as well as assessment and monitoring. In order to obtain significant information for biodiversity protection and management, a method based on the Soil Canopy Observation of Photosynthesis and Energy fluxes model and lookup table approach has been developed. The results derived from our study contain the reflectance values of *Scirpus mariqueter* and *Phragmites australis* spectra are lower than those commonly found for vegetated areas. This may be caused by the dark soil background and low LAI. Moreover, as for the values of latent heat flux (between 120 and 190 $\mathrm{W\,m^{-2}}$) and productivity (between 3 and 14 $\mu\mathrm{mol\,m^{-2}\,s^{-1}}$), mudflats are lower than vegetation. However, the values of sensible heat flux (between 140 and 170 $\mathrm{W\,m^{-2}}$) of mudflats are higher than that of vegetation. © *2021 Society of Photo-Optical Instrumentation Engineers (SPIE)* [DOI: 10.1117/1.JRS.15.038508]

1 Introduction

Tidal wetlands are significant and vulnerable aquatic ecosystems. They are present all around the world and serve as a kind of critical habitat for extensive varieties of fish, plants, and other wildlife.[1] This sort of ecosystem contributes to protecting and buffering shorelines, adjusting river runoff, controlling, and storing floodwaters potentially as well as purifying natural water bodies.[2] Moreover, as rapid growth of carbon dioxide from the air in recent years, tidal wetlands have become carbon sinks for atmospheric greenhouse gases due to the enormous carbon sequestration potential.[3] Nevertheless, these habitats are rapidly declining in area due to destruction by natural and human activities such as other species invasion,[4] sea-level rise,[5] and rapid urbanization.[6] Therefore, monitoring and protecting tidal wetlands, especially for coastal tidal wetlands, is important and valuable not only for ecosystem biodiversity but also for human sustainable development.

An effective wetland monitoring method for conservation and management should be integrated in nature, including multifarious significant aspects such as properties, distribution,

---

productivity, and components.[7,8] Nevertheless, conventional monitoring methods, which depend on sampling in field work to research characteristics of wetland, are usually time-consuming, expensive, and insufficient for analyzing the extensive regional difference and variability of time and space.[9] Remote sensing techniques using satellite sensors supplies an economical and convenient method to onerous field work for assessing, monitoring, and protecting coastal tidal wetland and its dynamic variations in different resolutions and scale levels.[10]

Over the past decade, developments in remote sensing techniques and rising availability of high-spectral and spatiotemporal resolution data have obviously improved our capacity to map properties of wetland habitats.[11] Multi-resolution spatiotemporal images from satellite such as MODIS, Landsat, and ASTER are available for free to the public and such sensors have been used in a few researches for the classification of wetland ecosystems.[12–14] Furthermore, some relatively high-resolution sensors just as Quickbird, SPOT, and RapidEye have been used by several studies for classification of dynamic detection analysis in wetland habitats.[15,16]

Remote sensing technique in wetland is more difficult than that of terrestrial vegetation due to the fact that coastal interface of wetland habitats that weakens the near-infrared (NIR) signal intensity, transfers red-edge locations, and eventually reduces effects of red-edge type indices and NDVI to detect growing vegetation.[17–19] Wetland habitats show relatively high-spatial and spectral variations as well because of the sudden changes of conditions in surrounding environments that generate limited ecotone areas, making plant community boundary identification difficult.[20] Vegetation diversity in wetland ecosystem generates diverse species combinations with various biochemical components and morphological structures, which, in reverse, produces different spectral performances resulting in difficulties in mapping of coastal tidal wetlands.[21,22] Also spectral overlaps make discrimination of green vegetation difficult.[14]

In recent years, some researches for monitoring and evaluating wetland habitats using remote sensing methods as well as varieties of image processing technologies have been concentrated on classification of vegetation communities[23,24] and depicting the scope of these ecosystems.[25,26] This sort of mapping supplies essential information about the spatial extent in the past and present and the dynamics changes of wetland coverage. Other remote sensing researches concentrate on analyzing and detecting the biophysical characteristics of coastal tidal wetland habitats using satellite sensors with coarse temporal resolution.[27,28] Although the research supplies profound scientific information of biophysical properties [such as leaf area index (LAI) and chlorophyll content (Cab)], they are always impossible to provide deeper understanding about the spatial variation of the tidal wetlands in wide coverage. Recently, a research developed mapping of tidal wetland biophysical properties for productivity dynamic changes analysis in the long term using MODIS through establishing relationship between VIs and biophysical characteristics.[29] However, this sort of mapping needs a lot of sampling data in different years and the process of field work is time-consuming.

Physically based modeling can be used to relate remote sensing signals to ecosystem characteristics. The Soil Canopy Observation of Photosynthesis and Energy (SCOPE) fluxes model, which is a representative soil-vegetation-atmosphere transfer approach combined with radiative transfer models for leaf and canopy,[30] has been used for the combined simulation of fluorescence signals, top of Canopy (TOC) reflectance, and thermal radiation with CO_2, energy, and water.[31] The SCOPE model that takes into account leaf biochemistry processes combining of radiative, mass transfers, and turbulent models inside the canopy is applied to surface energy balance, photosynthesis processes, and reflectance spectra between 400 and 50,000 nm.[32] In the visible wavelength range, reflectance reduces with increase in both chlorophyll and LAI values. Meanwhile, LE (latent heat flux), H (sensible heat flux), and gross primary productivity (GPP) are positively related to LAI and Cab so that LAI and Cab (and other pigments) can be used to simulate fluxes of H, LE, and GPP.

Chongming Dongtan coastal tidal wetland habitat is the largest estuary Alluvial Island and Sand Island in the world. And the Chongming Dongtan Nature Reserve was listed in the Chinese Protected Wetlands in the year of 1992, as well as regarded as internationally significant under the Ramsar Wetlands Convention in 2001 and also national nature preserve in the year of 2005.[33] In order to obtain significant information for biodiversity protection and management, the main objective of this study is to map of LAI, chlorophyll content, as well as the sensible heat flux, latent heat flux, and productivity in Chongming Dongtan coastal tidal wetland habitat of China
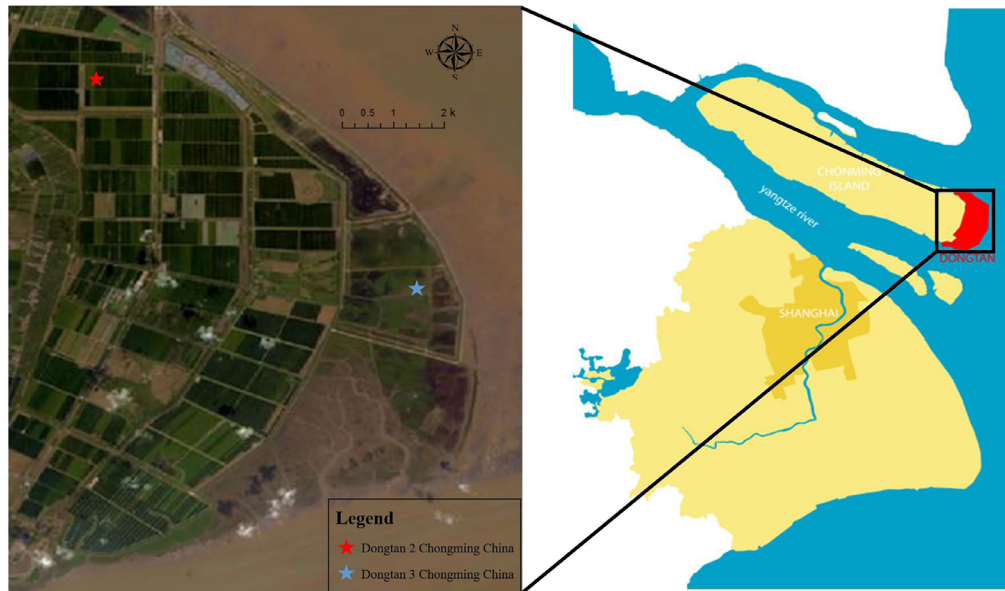
Fig. 1 Landsat 8 image of Chongming Dongtan wetlands in Shanghai on September 22, 2016 (locations of two flux towers: Dongtan 2 Chongming China and Dongtan 3 Chongming China).

through SCOPE model and lookup table approach using Landsat 8 data to help fill this knowledge gap.

2 Materials and Methodology

2.1 Study Area

Chongming Dongtan wetland habitat is located in the mouth of the Yangtze River Estuary in northeastern Shanghai, China (121°50′ to 122°05′ E, 31°25′ to 31°38′ N) (Fig. 1). It has an area of ~326 km^2 and it consists of marshland and tidal channels. And it has been regarded as a subtropical monsoon climate, with an average annual rainfall and temperature of 1022 mm and 15.3°C, respectively.[34]

There are several types of vegetation distributed in the study area such as *Scirpus mariqueter*, *Spartina alterniflora*, and *Phragmites australis* (from field investigation in September 2016). *Scirpus mariqueter* community dominates the vegetation at an elevation between 2 and 2.9 m in the salt marsh, whereas plant communities are dominated by *Phragmites australis* above 2.9 m.[33] As for *Spartina alterniflora*, it is a kind of invasive species that could be found on the most elevated soils higher than 3.5 m but its spatial distribution is not widespread.[33]

2.2 Study Materials

Landsat 8 Operational Land Imager (OLI) and thermal infrared sensor (TIRS) image on September 22, 2016 were selected for this study corresponding to the field data. Table 1 shows that the spatial resolution of Landsat 8 image for spectral bands 1 to 7 and 9 is 30 m. Landsat 5 Thematic Mapper (TM) images in the year between 2005 and 2007 were selected to validate simulated results corresponding to the flux tower data (2005 to 2007). The specific information of Landsat 5 TM sensor is illustrated in Table 1. Meteorological data in this research were used to complete atmospheric correction of the Landsat 8 OLI and TIRS image and Landsat 5 TM images. Meteorological data contained aerosol optical thickness, water vapor (g/cm^2), ozone (g atm cm), and surface pressure (hpa). They were collected from Meteorological Station website, Ozone and Air Quality website, and AERONET. The flux tower data in this research from the year 2005 to 2007 are all from two flux towers: Dongtan 2 Chongming China

Table 1 Band combinations of Landsat 8 OLI TIRS image and Landsat 5 TM image.

	Bands	Wavelength (μm)	Resolution (m)
Landsat 8 OLI and TIRS	Band 1: coastal aerosol	0.43 to 0.45	30
	Band 2: blue	0.45 to 0.51	30
	Band 3: green	0.53 to 0.59	30
	Band 4: red	0.64 to 0.67	30
	Band 6: SWIR 1	1.57 to 1.65	30
	Band 7: SWIR 2	2.11 to 2.29	30
	Band 8: panchromatic	0.50 to 0.68	15
	Band 9: cirrus	1.36 to 1.38	30
	Band 10: TIRS 1	10.60 to 11.19	100
	Band 11: TIRS 2	11.50 to 12.51	100
Launched February 11, 2013	Band 5: NIR	0.85 to 0.88	30
Landsat 5 TM	Band 1: blue	0.45 to 0.52	30
	Band 2: green	0.52 to 0.60	30
	Band 3: red	0.63 to 0.69	30
	Band 4: NIR	0.76 to 0.90	30
	Band 5: NIR	1.55 to 1.75	30
	Band 6: thermal	10.40 to 12.50	120
	Band 7: mid-infrared	2.08 to 2.35	30

Note: TIRS bands are acquired at 100 m resolution but are resampled to 30 m in delivered data product.

(31.5847° N, 121.9035° E) and Dongtan 3 Chongming China (31.5169° N, 121.9717° E) (Fig. 1). The flux tower data were all provided by State Key Laboratory of Estuarine and Coastal Research (SKLEC) and can supply listing of the variables [air temperature, wind speed, net ecosystem exchange (NEE), wind direction, CO_2 flux or the rate of vertical transfer of CO_2, sensible heat flux, latent heat flux, etc.], and they provide time series of sensible heat flux and latent heat flux. Without GPP processed (only NEE), this study was limited to H and LE. And measurement metadata (the information of locations, spectrum number, land cover types, vegetation height, vegetation fraction, soil moisture, and weather condition) were collected in September 2016.

2.3 Methodology

2.3.1 Data preprocessing of Landsat image

Data preprocessing has been performed to convert the level 1 Landsat 8 image to an atmospherically corrected image with TOC reflectance. To commence with, DN has been converted to reflectance in Integrated Land and Water Information System (ILWIS) using conversion guidelines and equations provided by USGS, for bands 1 to 9 of Landsat 8 OLI image containing the study area. In addition, atmospheric correction has been performed using the simplified method for the atmospheric correction (SMAC) toolbox in ILWIS using the data in Table 2. SMAC is a simplification of the code 6S[35] for atmospheric correction of visible- and near-visible bands of some satellite sensors.

Table 2 Necessary parameters and their data source of atmospheric correction.

No.	Input data for SMAC	Unit	Data source
1.	Aerosol optical thickness	—	AERONET website
2.	Water vapor	g/cm^2	AERONET website
3.	Ozone	g atm cm	Ozone and Air Quality website
4.	Surface pressure	hpa	Chinese Meteorological Station
5	Solar azimuth	deg	Landsat image products
6.	Solar zenith	deg	Landsat image products
7.	Sensor zenith	deg	Assumed NADIR
8.	Sensor azimuth	deg	0

2.3.2 *Model calibration with in situ data*

RTMo is the radiative transfer part of SCOPE for the visible to NIR.[36] After inputting the *in situ* reflectance, which was collected by ASD FieldSpec handheld 2 tool from field sampling into the RTMo retrievals of SCOPE model, the best estimates of vegetation and soil parameters were obtained. Meanwhile, the simulated reflectance spectra are also obtained. In order to reach the optimization of parameter sets, objective function has been selected to evaluate the results of the model calibration. The tools for the best fitting are already available at https://github.com/ christiaanvandertol. Subsequently, the retrieved parameters (Cab, LAI, and soil parameters) are obtained.

The objective function used for the retrieval was

$$\text{RMSE1} = \sqrt{\sum_{i=1}^{n} \frac{(\text{simulated reflectance} - in\ situ\ \text{reflectance})^2}{n}},$$

where RMSE1 is the root-mean-square error between simulated reflectance and *in situ* reflectance, n is the number of bands of *in situ* reflectance spectra, the simulated reflectance is the output reflectance of SCOPE model, and the *in situ* reflectance is the measured reflectance in the field.

2.3.3 *Simulated maps from SCOPE model with Landsat 8 data*

The SCOPE model simulated productivity, sensible heat flux, and latent heat flux correspond to respective reflectance data obtained based on iterative calculation of SCOPE algorithm. Using reflectance data and corresponding meteorological data, the productivity, sensible heat flux, and latent heat flux can be simulated by SCOPE model calibration, it is possible to estimate productivity, sensible heat flux, and latent heat flux from for example a Landsat 8 image:

$$\text{RMSE2} = \sqrt{\sum_{i=1}^{n} \frac{(\text{simulated reflectance} - \text{Landsat8 reflectance})^2}{n}},$$

where RMSE2 is the root-mean-square error between simulated reflectance and Landsat 8 reflectance, and n is the number of bands of Landsat 8 image. Simulated reflectance is the output reflectance of SCOPE model converting into Landsat 8 OLI bands (the first seven bands) after calibration and Landsat 8 reflectance is the TOC reflectance from Landsat 8 OLI image.

2.3.4 Model validation

Without GPP processed (only NEE) from flux tower data, this study was limited to sensible heat flux and latent heat flux for model validation. First of all, it is necessary to repeat the steps in Sec. 2.3.3 to get the simulations of sensible heat flux, latent heat flux, and the corresponding soil spectra, LAI, and chlorophyll content in the year from 2005 to 2007 using Landsat 5 images. Meanwhile, soil spectra, LAI, and chlorophyll around flux tower from simulations can be selected through the above simulations. Then the time series of sensible heat flux and latent heat flux were simulated with the time series module of SCOPE model with the value of the above soil spectra, LAI, and chlorophyll around the flux tower.

Furthermore, the measured time series of sensible heat flux and latent heat flux were compared to field measurements. (The flux tower data for the year from 2005 to 2007 were available at SKLEC.) Then model validation was carried out through comparing the two curves mentioned above using objective function as follows:

$$\text{RMSE3} = \sqrt{\sum_{i=1}^{n} \frac{(\text{simulated results} - \text{flux tower data})^2}{n}},$$

where RMSE3 is the root-mean-square-error between simulated results and flux tower data, n is the number of measuring records. Simulated results include the sensible heat flux, productivity, and latent heat flux from time series module of SCOPE model in the year from 2005 to 2007, using Landsat 5 TM images and flux tower data is the corresponding sensible heat flux, productivity, and latent heat flux collected from 2005 to 2007 at SKLEC.

3 Results

3.1 Analysis of Model Calibration with Measurements and Simulations

The objective of this section is to calibrate the measuring data with the simulation ones to select the best vegetation parameters as the input data in SCOPE model simulations through adjusting parameter values with some prior information.[37,38]
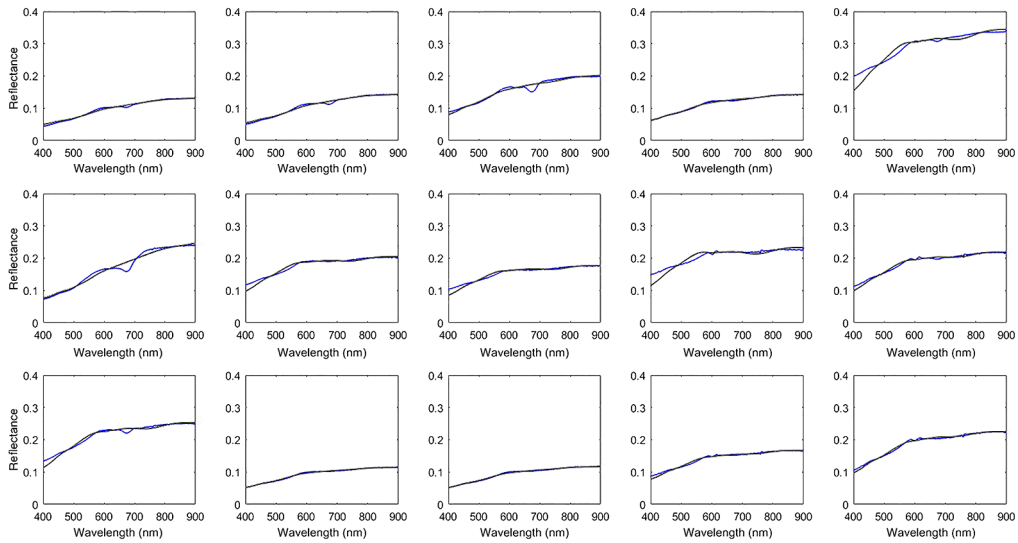
3.1.1 Mudflats

RTMo (transfer of solar and sky radiation) retrievals of SCOPE model should be used for this section. For the mudflats, the LAI was set to zero (no vegetation) and then the soil parameters [soil brightness (B), parameters that determine the shape of the soil reflectance spectrum excluding soil brightness (lat and lon), and soil moisture content (SMp), which mostly affects the soil brightness] are varied to obtain the optimization of soil parameters and simulations for each sample points (Fig. 2). As all the 15 graphs of mudflats spectra shown, the measurements matched the simulations pretty well. Especially, the total one (Fig. 3) that represented the RTMo results and measured data were fairly satisfying excluding the final noise (reflectance after 900 nm). Meanwhile, the RMSE values between the simulations and measuring data for each sample point are all below 0.014, and its mean value is 0.00524.
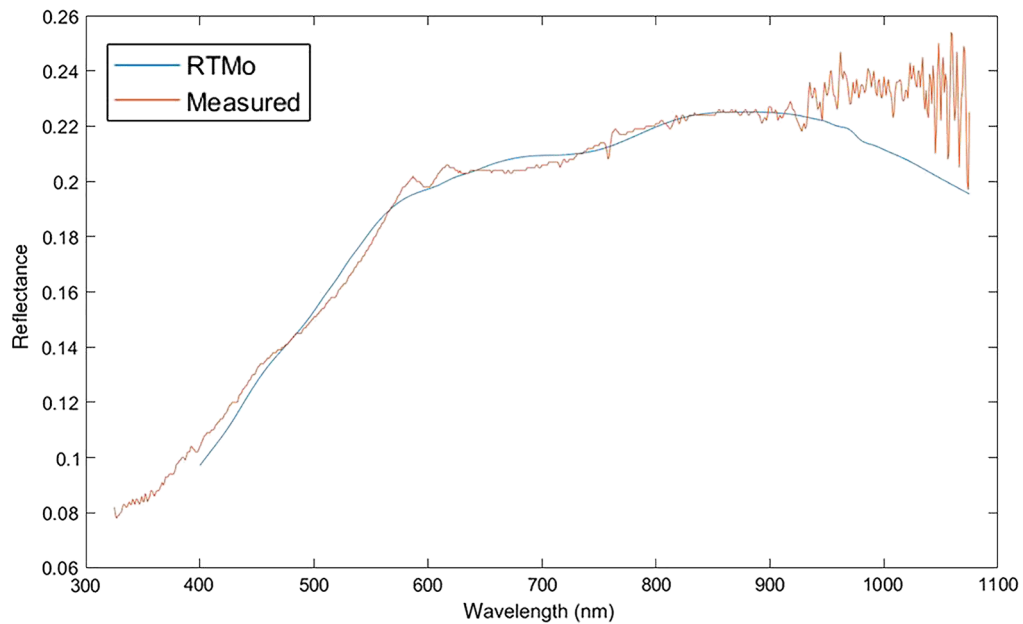
Table 3 depicts the maximum, minimum, and mean values of those four soil parameters after simulations of RTMo retrievals. The mean values of those four soil parameters are selected as the soil basic values in RTMo retrievals of SCOPE model.

3.1.2 Vegetation

Based on the above results of mudflats, four soil parameters were treated as constant for the vegetated areas and the vegetation parameters [the chlorophyll concentration of the leaves (Cab), the carotenoid concentration of the leaves (Cca), dry matter concentration of the leaves (Cmd), the water concentration of the leaves (Cw), senescent material content (Cs), the mesophyll thickness parameter (N), the leaf inclination parameter (LIDFa), the bimodality of the

Fig. 2 The simulated (gray line) and measuring (blue line) reflectance spectra of mudflats in each sample point.

Fig. 3 The total simulated and measuring reflectance spectra of mudflats.

Table 3 The maximum, minimum, and mean values of four soil parameters in RTMo retrievals.

Parameters	Maximum	Minimum	Mean
B	0.8187	0.3042	0.5354
lat	28.7078	23.2313	26.9000
lon	44.8608	17.5263	29.8265
SMp	51.4208	14.7901	43.1477

leaf inclination (LIDFb), and the LAI] were retrieved. According to the types of vegetation (*Phragmites australis, Scirpus mariqueter*, and *Spartina alterniflora*), simulations of vegetation parameters were divided into three parts as Fig. 4 describes. All of them were quite satisfying due to the fact that the simulations matched measurements quite well in the wavelength range between 400 and 900 nm. As for the value of RMSE between simulations and measurements, *Phragmites australis* is no more than 0.004, *Scirpus mariqueter* is no more than 0.005, and *Spartina alterniflora* is no more than 0.008. Thus the spectra were well reproduced after the calibration. However, independent leaf measurements were available to validate whether the retrieved parameters were correct.

Table 4 illustrates the maximum, minimum, and mean values of nine vegetation parameters for three vegetation types after retrievals using RTMo. The mean values of six vegetation parameters (Cmd, Cw, Cs, N, LIDFa, and LIDFb) for three vegetation types, and the mean values of the above four soil parameters (B, lat, lon, and SMp) were selected as the input data in the next step of SCOPE model simulation: the generation of the lookup table for retrievals from Landsat 8.

3.2 Mapping of Productivity, Latent Heat Flux, Sensible Heat Flux, and Vegetation Parameters

As we can see from Fig. 5, chlorophyll pigment concentration in coastal tidal wetlands in image is between 5 and 60 μg cm^{-2} and those who have higher concentration are resembles to agriculture farms or parks in the whole map. As for the masked part in chlorophyll map, it represents the masked area of which RMSE > 0.05. The reasons for the strange phenomenon can be explained in Sec. 4. Meanwhile, LAI in coastal tidal wetland in image is no more than 2.0 m^2 m^{-2} and those who have higher constant LAI values (more than 2.5 m^2 m^{-2}) resemble to agriculture farms and parks in image. Moreover, the map of productivity flows mostly the same trend as of LAI in coastal tidal area. It can be confirmed from the map of productivity and LAI that the area with high LAI has a higher productivity. Last but not least, the latent heat flux is between 90 and 150 W m^{-2} in coastal tidal wetland part, whereas the sensible heat flux is almost between 140 and 170 W m^{-2}. Also the sensible heat flux of vegetated areas in coastal tidal wetland is lower than that of mudflats.

## 3.3 Results of Model Validation with Simulations and Measurements

Based on the above section, fluxes were simulated for the whole September of the 3 years. Thus SCOPE model was executed for 6 times, assuming that the retrieved Cab and LAI could be considered representative for a month. And then the simulated time series of latent heat flux and sensible heat flux in September from 2005 to 2007 were obtained. The simulated and measured curves of latent heat flux and sensible heat flux in the two flux towers in the year of 2005 were described in Figs. 6 and 7 (the curves in 2006 and 2007 were similar). The records of flux tower measurements during rainy days were removed, because during those days, the reliable data could not be obtained. As seen from the following figures, the simulated data have little difference with the actually measured data, which indicated that the results of model simulation are effective.

4 Discussion

4.1 Analysis of Selecting Variable Value Range of Input Parameters in SCOPE Model Simulation

Selection of input data (Cab, Cca, LAI, soil spectra number, etc.) range in SCOPE model influences the final simulations of mapping profoundly. The simulated maps of productivity, latent heat flux, sensible heat flux, LAI, and chlorophyll can be obtained as Fig. 8(a) illustrates through individual run of SCOPE model with all the parameters of 46 measuring points as input data in the LUT. Although RMSE value is no more than 0.05 along coastal tidal wetland,
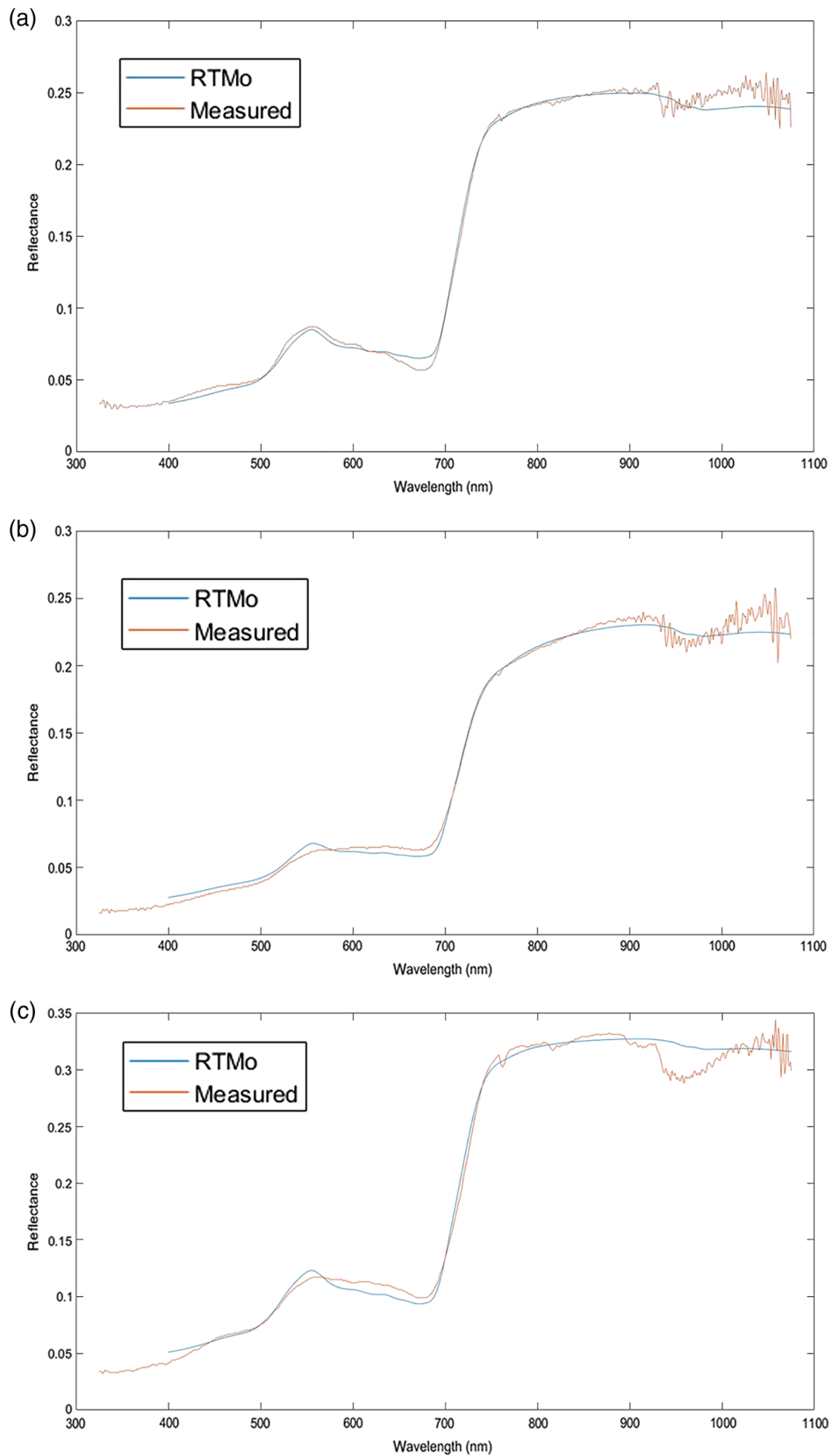
Fig. 4 The total curves between simulations and measurements of three vegetation types: (a) *Phragmites australis*, (b) *Scirpus mariqueter*, and (c) *Spartina alterniflora.*

Table 4 The maximum, minimum, and mean values of nine vegetation parameters for three vegetation types in RTMo retrievals.

| Parameters	*Phragmites australis*			*Scirpus mariqueter*			*Spartina alterniflora*		
	Maximum	Minimum	Mean	Maximum	Minimum	Mean	Maximum	Minimum	Mean
Cab (μg cm^{-2})	56	21	31	59	15	29	59	37	52
Cw (g cm^{-2})	0.0213	0.0152	0.0184	0.0322	0.0159	0.0228	0.0180	0.0135	0.0151
Cmd (g cm^{-2})	0.0121	0.0002	0.0059	0.0200	0.0002	0.0132	0.0069	0.0001	0.0024
Cs (a.u.)	0.3073	0.0601	0.2000	0.3996	0.0128	0.2258	0.2105	0.0850	0.1288
Cca (μg cm^{-2})	10.5	6.2	8.6	11.4	7.4	9.4	13.7	9.2	11.7
N (dimensionless)	2.27	1.06	1.45	2.07	1.00	1.17	3.46	1.50	2.78
LAI (m^2 m^{-2})	1.56	0.99	1.35	2.38	0.34	1.74	2.51	0.43	1.23
LIDFa	−0.1401	−0.9802	−0.7128	0.0788	−1.0000	−0.8820	0.7117	−0.5570	0.2272
LIDFb	−0.0048	−0.1637	−0.1130	0.0068	−0.1283	−0.0321	−0.0518	−0.1337	−0.0821
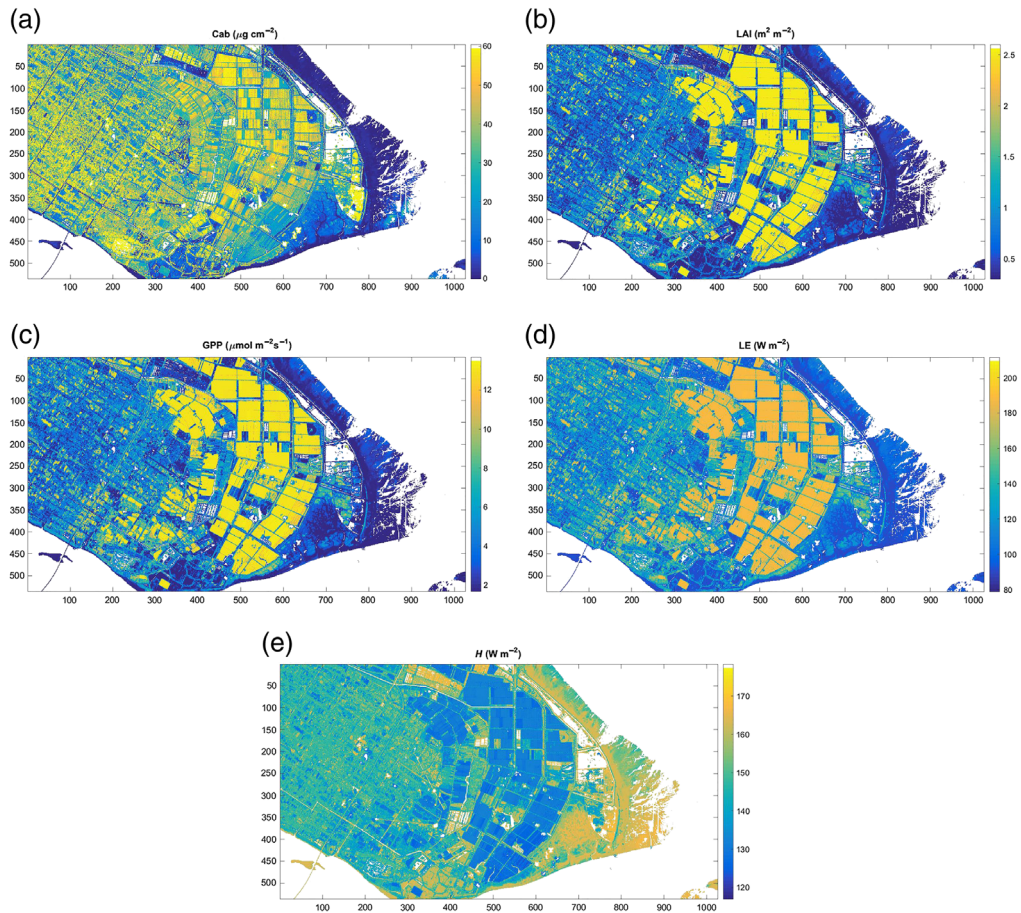
Fig. 5 Map of biophysical and biochemical properties in Chongming Dongtan: (a) leaf chlorophyll content (μg cm^{-2}), (b) LAI (m^2 m^{-2}), (c) productivity (μmol m^{-2} s^{-1}), (d) latent heat flux (W m^{-2}), and (e) sensible heat flux (W m^{-2}).
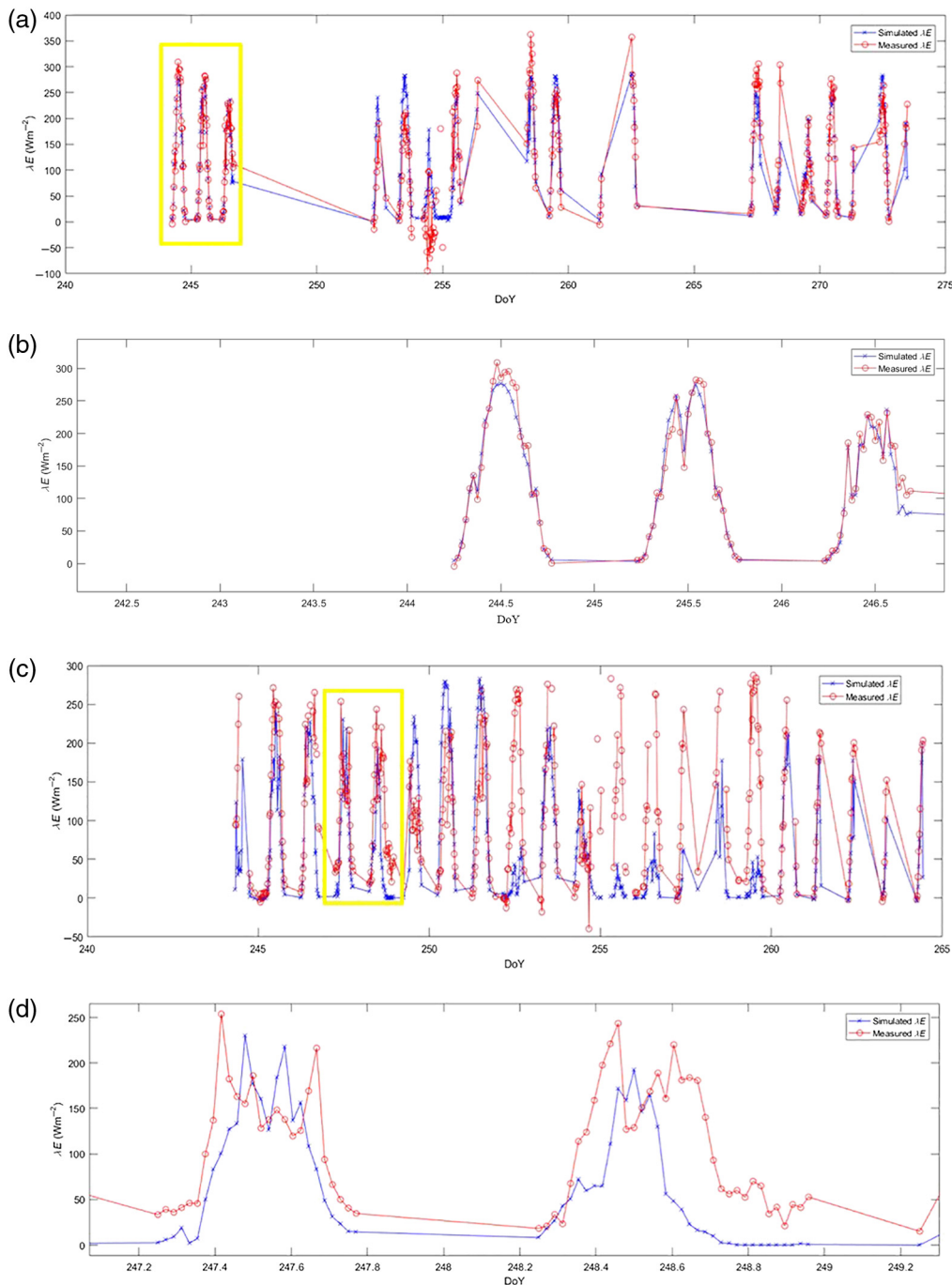
Fig. 6 The simulated and measured curves of latent heat flux in the year of 2005: (a) Dongtan 2, (b) larger version of the yellow rectangle in (a), (c) Dongtan 3, and (d) larger version of the yellow rectangle in (c).
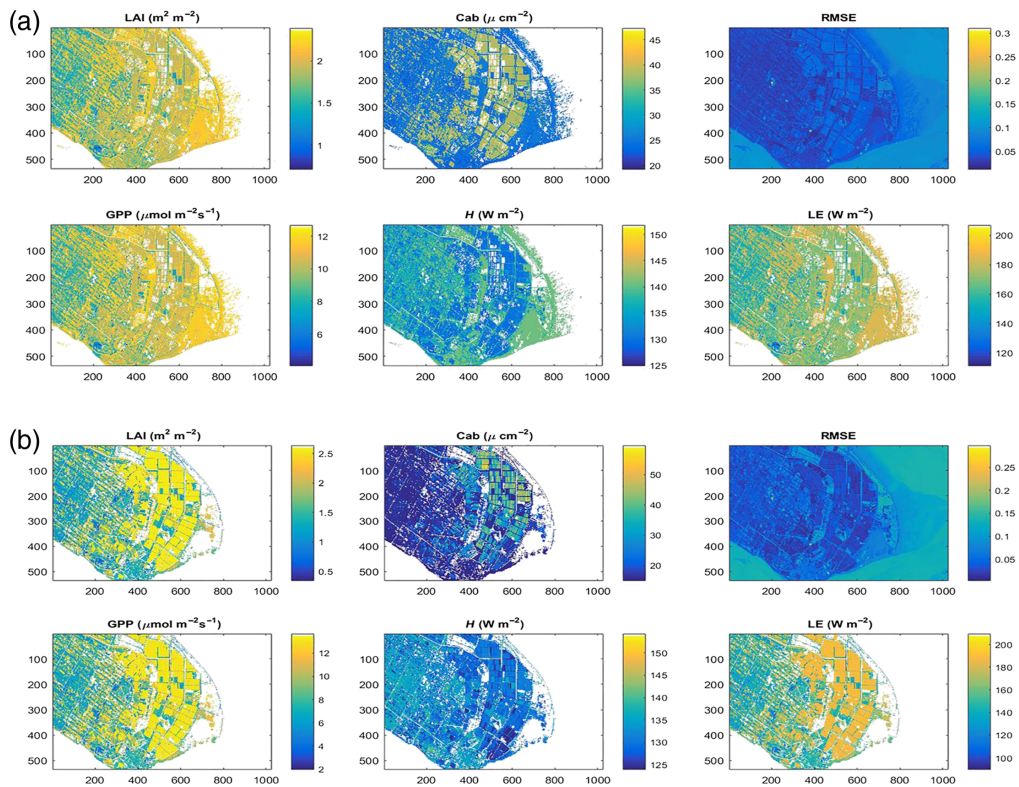
the values of productivity, latent heat flux, sensible heat flux, LAI, and chlorophyll in coastal tidal wetland are not changed so much. However, actually mudflats account for a large part of wetland in September. Therefore, the values of LAI and chlorophyll should not be high and similar along coastal tidal wetland. An LUT of only 46 combinations cannot represent the whole area well. As for the combination of LAI and chlorophyll without 0 value [Fig. 8(b)], the simulated maps are better than those of the combination of 46 measuring points. However, the mudflats were also not simulated satisfyingly. The cause is that the simulation has not contained mudflats' properties and SCOPE cannot simulate well in such conditions.
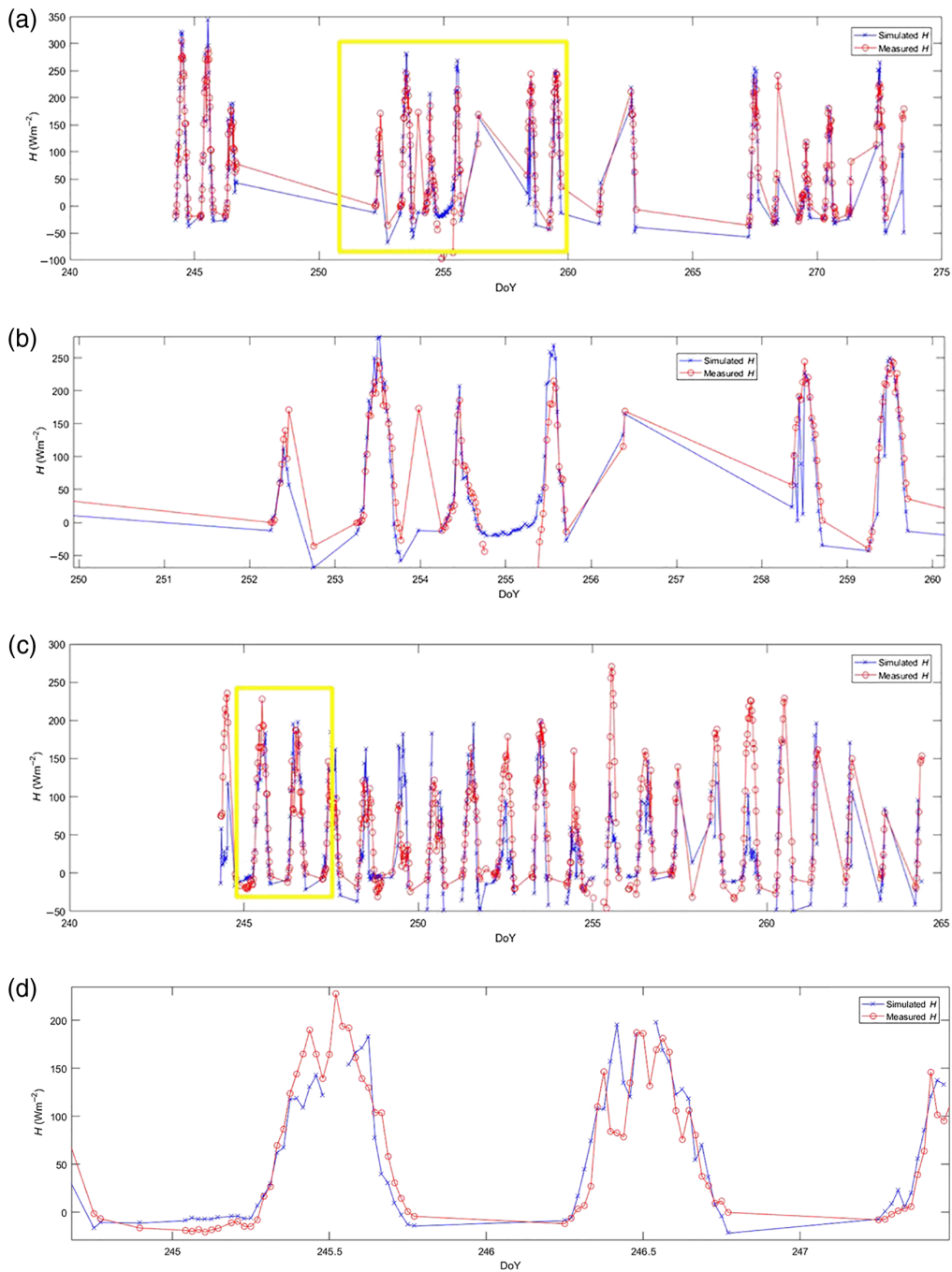
Fig. 7 The simulated and measured curves of sensible heat flux in the year of 2005: (a) Dongtan 2, (b) larger version of the yellow rectangle in (a), (c) Dongtan 3, and (d) larger version of the yellow rectangle in (c).

4.2 *Reasons for the Uncertainties of Mapping with SCOPE Model*

Based on Sec. 3.3, there was masked part in simulated maps of productivity, latent heat flux, sensible heat flux, LAI, and chlorophyll for which RMSE of the simulated Landsat 8 OLI reflectance exceeded 0.05. As for the reasons for removing the parts of which RMSE value is more than 0.05 can be found in comparing Landsat 8 OLI image in natural color composite with the simulated maps before removing (Fig. 9). Actually LAI value in the mudflats and ocean parts should be 0, but they had nonzero value in the simulated LAI map. Therefore, the incorrect part

Fig. 8 The simulated maps of productivity, latent heat flux, sensible heat flux, LAI, chlorophyll, and RMSE with combination: (a) 46 measuring points and (b) LAI and chlorophyll without 0 value.
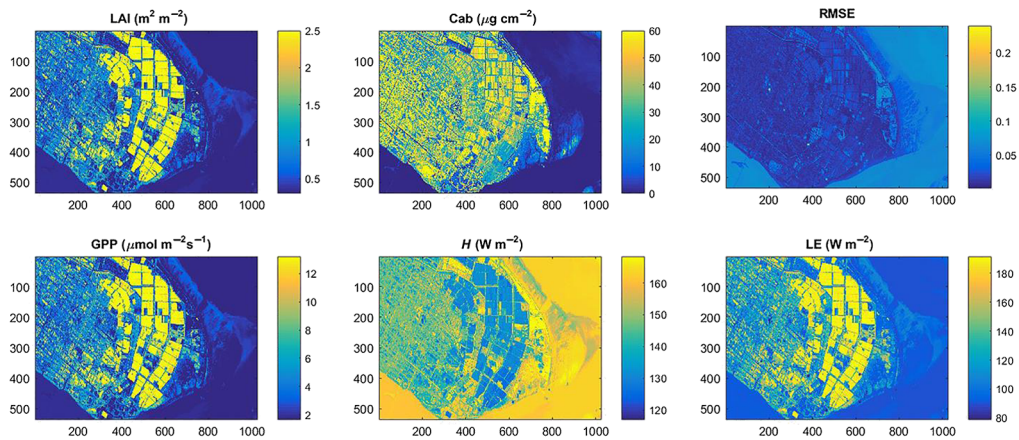
Fig. 9 The simulated maps of productivity, latent heat flux, sensible heat flux, LAI, chlorophyll, and RMSE before removing.

should be removed. When RMSE value is more than 0.05, the clouds, unrealistic mudflat, and ocean parts can be all masked. Therefore, a limit of RMSE of 0.05 was used.

To be more specific, we can select two points [one is in vegetated area (RMSE < 0.02), and the other is in mudflats (RMSE > 0.1)] in the simulated map to analyze the simulated accuracy of different areas. From Fig. 10(a), the results of five simulated reflectance spectra and pixel values in seven bands of Landsat 8 in vegetated area is relatively consistent. However, the model simulations and pixel values in seven bands of Landsat 8 in mudflats from Fig. 10(b) are completely different. In brief, through comparing the specific simulations of two points, the reasons for the uncertainties of SCOPE model simulations can be inferred as follows:[5] meteorological influence;[4] insufficiency of input data of soil properties;[23] the quality and
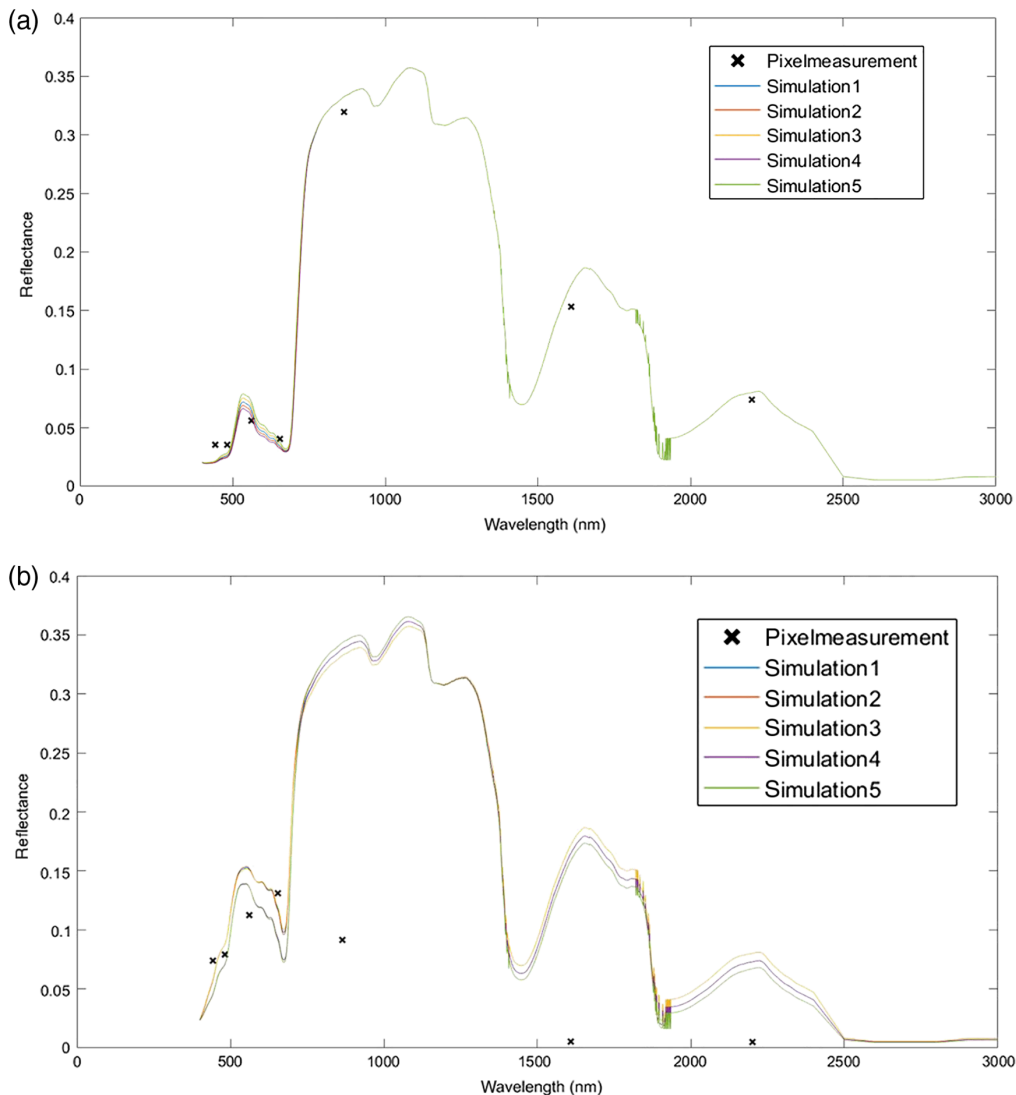
Fig. 10 The five simulated reflectance spectra and pixel values in seven bands of Landsat 8 in different areas: (a) vegetated area and (b) mudflats area.

quantity of field work data;[9] and the number of simulated combinations. If the above problems can be improved, the simulated results could improve.

5 Conclusions

Initially, in the case of the differences of *in situ* measured spectral signatures of the different vegetation types and the mudflats, the reflectance values of *Scirpus mariqueter* and *Phragmites australis* spectra are lower than those commonly found for vegetated areas. This may be caused by the dark soil background and low LAI. Moreover, in terms of LAI and chlorophyll value, mudflats should be 0, whereas the counterparts of vegetation are around 1 to 2 $m^2\,m^{-2}$ and 5 to 60 $\mu g\,cm^{-2}$, respectively. As for the values of latent heat flux and productivity, mudflats are lower than vegetation. However, the values of sensible heat flux of mudflats are higher than that of vegetation. Last but not least, the uncertainties of the productivity (photosynthesis) product of the SCOPE model from Landsat 8 are:[5] uncertain meteorological condition (only an example of meteorological condition in SCOPE input data, not the real weather for study area);[4] insufficient simulation of mudflats;[23] the quality and quantity of field work data;[9] and the number of simulated combinations.

For further study, if the quality and quantity of field work data can be improved, the results of mapping protocol of biophysical and biochemical properties in Chongming Dongtan wetland for environmental protection and restoration as well as assessment and monitoring will be much better. Furthermore, this work gives good suggestions related to quantifying present or future biophysical and biochemical properties of ecosystem, at least in coastal tidal wetland habitats, through multi-spectral satellite data.

Acknowledgments

References

1. K. R. Turpie et al., "Prospective HyspIRI global observations of tidal wetlands," *Remote Sens. Environ.* **167**, 206–217 (2015).
2. N. Levin, E. Elron, and A. Gasith, "Decline of wetland ecosystems in the coastal plain of Israel during the 20th century: implications for wetland conservation and management," *Landscape Urban Plann.* **92**(3–4), 220–232 (2009).
3. Y. Hu et al., "Salinity and nutrient contents of tidal water affects soil respiration and carbon sequestration of high and low tidal flats of Jiuduansha wetlands in different ways," *Sci. Total Environ.* **565**, 637–648 (2016).
4. J. Chen et al., "Effect of *Spartina alterniflora* invasion and its controlling technologies on soil microbial respiration of a tidal wetland in Chongming Dongtan, China," *Ecol. Eng.* **41**, 52–59 (2012).
5. M. J. A. N. Bhuiyan and D. Dutta, "Analysis of flood vulnerability and assessment of the impacts in coastal zones of Bangladesh due to potential sea-level rise," *Nat. Hazards* **61**(2), 729–743 (2012).
6. J. H. Tian et al., "A conceptual ecological model of Cangzhou coastal wetlands, Hebei Province, China," *Procedia Environ. Sci.* **2**, 1002–1011 (2010).
7. K. Tuxen et al., "Mapping changes in tidal wetland vegetation composition and pattern across a salinity gradient using high spatial resolution imagery," *Wetlands Ecol. Manage.* **19**, 141–157 (2011).
8. C. Lu et al., "Monitoring and assessment of wetland loss and fragmentation in the cross-boundary protected area: a case study of Wusuli River basin," *Remote Sens.* **11**(21), 2581 (2019).
9. T. I. R. de Almeida et al., "Principal component analysis applied to a time series of MODIS images: the spatio-temporal variability of the Pantanal wetland, Brazil," *Wetlands Ecol. Manage.* **23**(4), 737–748 (2015).
10. C. Wigand et al., "Development and validation of rapid assessment indices of condition for coastal tidal wetlands in southern New England, USA," *Environ. Monit. Assess.* **182**(1–4), 31–46 (2011).
11. M. S. Gilmore et al., "Integrating multi-temporal spectral and structural information to map wetland vegetation in a lower Connecticut River tidal marsh," *Remote Sens. Environ.* **112**(11), 4048–4060 (2008).
12. E. J. J. Sieben et al., "The vegetation of inland wetlands with salt-tolerant vegetation in South Africa: description, classification and explanatory environmental factors," *S. Afr. J. Bot.* **104**, 199–207 (2016).
13. G. Tana et al., "Wetlands mapping in North America by decision rule classification using MODIS and ancillary data," *IEEE J. Sel. Top. Appl. Earth Obs. Remote Sens.* **6**(6), 2391–2401 (2013).

14. S. M. R. Alam and M. S. Hossain, "A rule-based classification method for mapping Saltmarsh land-cover in south-eastern Bangladesh from Landsat-8 OLI," *Can. J. Remote Sens.* **47**, 356–380 (2020).

15. S. H. Hong et al., "Evaluation of polarimetric SAR decomposition for classifying wetland vegetation types," *Remote Sens.* **7**(7), 8563–8585 (2015).

16. Z. Wentao et al., "Texture classification of vegetation cover in high altitude wetlands zone," *Conf. Ser. Earth Environ. Sci.* **17**, 012083 (2014).

17. C. Guo and X. Guo, "Estimating leaf chlorophyll and nitrogen content of wetland emergent plants using hyperspectral data in the visible domain," *Spectrosc. Lett.* **49**(3), 180–187 (2016).

18. O. Mutanga, E. Adam, and M. A. Cho, "High density biomass estimation for wetland vegetation using worldview-2 imagery and random forest regression algorithm," *Int. J. Appl. Earth Obs. Geoinf.* **18**(1), 399–406 (2012).

19. D. Siciliano et al., "Evaluating hyperspectral imaging of wetland vegetation as a tool for detecting estuarine nutrient enrichment," *Remote Sens. Environ.* **112**(11), 4020–4033 (2008).

20. K. Prospere, K. McLaren, and B. Wilson, "Plant species discrimination in a tropical wetland using in situ hyperspectral data," *Remote Sens.* **6**(9), 8494–8523 (2014).

21. B. W. Heumann, R. A. Hackett, and A. K. Monfils, "Testing the spectral diversity hypothesis using spectroscopy data in a simulated wetland community," *Ecol. Inf.* **25**, 29–34 (2015).

22. B. W. Pengra, C. A. Johnston, and T. R. Loveland, "Mapping an invasive plant, *Phragmites australis*, in coastal wetlands using the EO-1 Hyperion hyperspectral sensor," *Remote Sens. Environ.* **108**(1), 74–81 (2007).

23. X. Chonglin, "Mapping wetland vegetation and estimating its biophysical characteristics using C-band ENVISAT ASAR in Poyang Lake, China" (2009).

24. C. Wright and A. Gallant, "Improved wetland remote sensing in Yellowstone National Park using classification trees to combine TM imagery and ancillary environmental data," *Remote Sens. Environ.* **107**(4), 582–605 (2007).

25. I. Dronova, P. Gong, and L. Wang, "Object-based analysis and change detection of major wetland cover types and their classification uncertainty during the low water period at Poyang Lake, China," *Remote Sens. Environ.* **115**(12), 3220–3236 (2011).

26. A. Goudie, "Characterising the distribution and morphology of creeks and pans on salt marshes in England and Wales using Google Earth," *Estuarine Coastal Shelf Sci.* **129**, 112–123 (2013).

27. D. R. Mishra et al., "Post-spill state of the marsh: remote estimation of the ecological impact of the Gulf of Mexico oil spill on Louisiana Salt Marshes," *Remote Sens. Environ.* **118**, 176–185 (2012).

28. D. R. Mishra et al., "Wetland mapping methods and techniques using multisensor, multi-resolution remote sensing: successes and challenges," *Remote Sensing of Water Resources, Disasters, and Urban Studies*, P. Thenkabail, Ed., pp. 191–226, CRC Press, Boca Raton, Florida (2015).

29. S. Ghosh, D. R. Mishra, and A. A. Gitelson, "Long-term monitoring of biophysical characterisics of tidal wetlands in the northern Gulf of Mexico—a methodological approach using MODIS," *Remote Sens. Environ.* **173**, 39–58 (2016).

30. C. van der Tol et al., "An integrated model of soil-canopy spectral radiances, photosynthesis, fluorescence, temperature and energy balance," *Biogeosciences* **6**(12), 3109–3129 (2009).

31. J. Timmermans et al., "Quantifying the uncertainty in estimates of surface-atmosphere fluxes through joint evaluation of the SEBS and SCOPE models," *Hydrol. Earth Syst. Sci.* **17**(4), 1561–1573 (2013).

32. C. Duffour et al., "An evaluation of SCOPE: a tool to simulate the directional anisotropy of satellite-measured surface temperatures," *Remote Sens. Environ.* **158**, 362–375 (2015).

33. Z. Zheng et al., "The spatial relationship between salt marsh vegetation patterns, soil elevation and tidal channels using remote sensing at Chongming Dongtan Nature Reserve, China," *Acta Oceanolog. Sin.* **35**(4), 26–34 (2016).

34. Y. A. Zou et al., "Migratory waterbirds response to coastal habitat changes: conservation implications from long-term detection in the Chongming Dongtan Wetlands, China," *Estuaries Coasts* **39**(1), 273–286 (2016).

35. H. Rahman and G. Dedieu, "SMAC: a simplified method for the atmospheric correction of satellite measurements in the solar spectrum," *Int. J. Remote Sens.* **15**(1), 123–143 (1994).
36. C. Van Der Tol et al., "A model and measurement comparison of diurnal cycles of sun-induced chlorophyll fluorescence of crops," *Remote Sens. Environ.* **186**, 663–677 (2016).
37. W. Lin and N. Chen, "Inversion of leaf area index for invasive plant using ENVISAT ASA," Urban Remote Sensing Joint Event (2009).
38. Q. Zhong et al., "Carbon dioxide fluxes and their environmental control in a reclaimed coastal wetland in the Yangtze Estuary," *Estuaries Coasts* **39**, 344–362 (2016).

Nanhuanuowa Zhu received her Master of Science degree from the Faculty of Geo-information Science and Earth Observation, University of Twente, Twente, Netherlands. She mainly engaged in assessment of non-point source pollution in watershed scale. Now, she is an intermediate engineer at Satellite Application Center for Ecology and Environment, Ministry of Ecology and Environment, Beijing, China.

Biographies of the other authors are not available.